Dual-energy subtraction for contrast-enhanced digital breast tomosynthesis

Ann-Katherine Carton* a), Karin Lindman b), Christer Ullberg b), Tom Francke b),
Andrew D.A. Maidment a)
a) University of Pennsylvania, Philadelphia PA, USA
b) XCounter AB, Svardvagen 11, SE-182 33 Danderyd, Sweden
{Ann-Katherine.Carton | Andrew.Maidment} @uphs.upenn.edu
{Karin.Lindman | Christer.Ullberg|Tom.Francke} @xcounter.se

ABSTRACT

We have developed a dual-energy subtraction technique for contrast-enhanced breast tomosynthesis. The imaging system consists of 48 photon-counting linear detectors which are precisely aligned with the focal spot of the x-ray source. The x-ray source and the digital detectors are translated across the breast in a continuous linear motion; each linear detector collects an image at a distinct angle. A pre-collimator is positioned above the breast and defines 48 fan-shaped beams, each aligned with a detector. Low- and high-energy images are acquired in a single scan; half of the detectors capture a low-energy beam and half capture a high-energy beam, as alternating fan-beams are filtered to emphasize low and high energies. Imaging was performed with a W-target at 45 and 49 kV. Phantom experiments and theoretical modeling were conducted. Iodine images were produced with weighted logarithmic subtraction. The optimal tissue cancellation factor, w_t, was determined based on simultaneous preservation of the iodine signal and suppression of simulated anatomic background. Optimal dose allocation between low- and high-energy images was investigated. Mean glandular doses were restricted to ensure clinical relevance. Unlike other dual-energy approaches, both spectra must have the same peak energy in this system design. We have observed that w_t is mainly dependent on filter combination and varies only slightly with kV and breast thickness, thus ensuring a robust clinical implementation. Optimal performance is obtained when the dose fraction allocated to the high energy images ranges from 0.55 to 0.65. Using elemental filters, we have been able to effectively suppress the anatomic background.

Keywords: DE, TSYN, MG

1. INTRODUCTION

Breast tumor growth and metastasis are accompanied by the development of new blood vessels that have an abnormally increased permeability[1]. As a result, the absorption of vascular contrast agents is often different in cancerous tissue than in benign and normal breast tissues.

This aspect of breast cancer biology has been demonstrated by several imaging techniques using a vascular contrast agent. Since its introduction in 1986, contrast-enhanced breast magnetic resonance imaging (CE-MRI), a 3-dimensional technique with a gadolinium-based contrast agent, has been the most widely used clinical technique[2-5]. In the 1980s, there was also considerable research on x-ray imaging techniques combined with an iodine vascular contrast agent to demonstrate breast cancers[6-9]. Contrast-enhanced computed tomography (CE-CT)[8], CE digital subtraction angiography[6,7] (CE-DSA) and CE mammography[9] (CE-M) have been considered. However, these technologies were not practical for routine clinical practice due to limited spatial resolution (CE-CT, CE-DSA), high patient dose (CE-CT), limited x-ray tube loading (CE-M), and impractical image handling (CE-M).

The recent availability of high-speed readout, high spatial resolution and low-dose full-field digital mammography (FFDM), digital breast tomosynthesis (DBT), and dedicated breast CT systems has triggered renewed interest in the development of x-ray techniques for CE-breast imaging[10-13].

* Phone 1 215 746 8759 -- Fax 1 215 746 8764

Medical Imaging 2007: Physics of Medical Imaging, edited by Jiang Hsieh, Michael J. Flynn,
Proc. of SPIE Vol. 6510, 651007, (2007) · 1605-7422/07/$18 · doi: 10.1117/12.713703

The tomographic nature of CE-DBT makes CE-DBT superior to CE-FFDM and suggests that CE-DBT has the potential to rival CE-MRI. Our first years' experience with *temporal-subtraction* CE-DBT (where high-energy images are acquired before and after administration of an iodine contrast agent), taught us that quantification of contrast-agent uptake is practically impossible, primarily because of patient motion between the pre-and post-contrast series[14].

In this work, we will present a *dual-energy contrast-enhanced* (DECE) *subtraction* technique[11,12] optimized for DBT. This technique is known to overcome the artifacts due to patient motion[15]. In DECE-DBT; the iodine contrast agent is injected and then two images, one containing an x-ray spectrum below the k-edge of iodine and one at higher energy, are acquired in rapid succession at each time point. Then, a weighted difference between the low- and high-energy breast images is calculated. By exploiting the differences in the energy dependence of attenuation of breast tissue (*i.e.* glandular and fatty tissue) and iodine, images emphasizing breast signal or iodine signal can be produced.

We have developed a DECE-DBT technique using a photon-counting DBT imaging system. In our system design, the high- and low-energy images are acquired in a single scan. We have conducted both phantom experiments and theoretical modeling to optimize system design and determine the technical acquisition parameters.

2. IMAGING SYSTEM DESIGN

DECE-DBT images were acquired with a photon counting DBT system (XC Mammo-3T, XCounter AB, Danderyd, Sweden). The imaging system consists of 48 photon-counting linear detectors which are precisely aligned with the focal spot of the x-ray source. The x-ray source and the digital detectors are translated across the breast in a continuous linear motion; each linear detector collects a projection image at a distinct angle. A pre-collimator is positioned above the breast and defines 48 fan-shaped beams, each aligned with a detector. Low- and high-energy images are acquired in a single scan; half of the detectors capture a low-energy beam and half capture a high-energy beam, as the 48 fan-shaped beams are alternately filtered to emphasize low and high energies. We have investigated the use of 0.185, 0.356 and 0.490 mm Sn and 135 mg I/cm^2 + 1 cm H_2O, 225 mg I/cm^2 + 0.875 cm H_2O and 305 mg I/cm^2 + 0.875 cm H_2O filters for the low-energy x-ray spectrum. Cu filters with 0.107, 0.212 and 0.270 mm thickness were investigated for the high-energy x-ray spectrum. Imaging was performed using a W-target at 45 kV and 49kV. Figure 1 illustrates low- and high-energy spectra obtained by filtering a 49 kV W-target x-ray beam with 0.356 mm Sn, 225 mg I/cm^2 and 0.212 mm Cu. The spectra were simulated using a validated extrapolation of Boone's model[16].

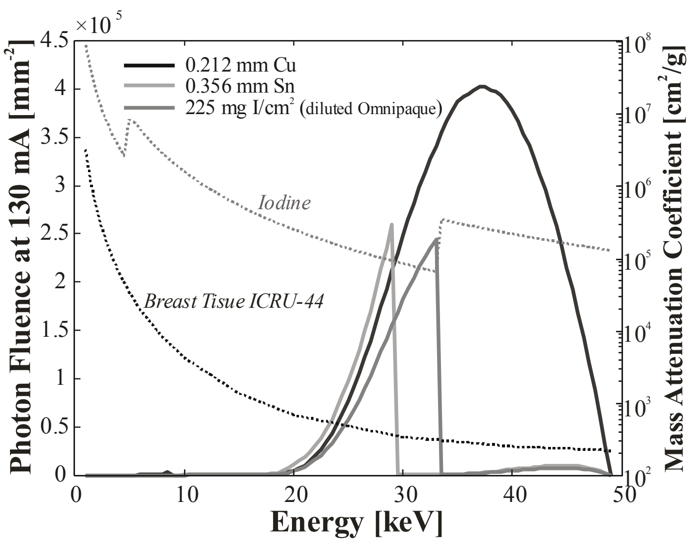

Figure 1: Mass attenuation coefficients of iodine and ICRU-44 breast tissue. Examples of simulated low-energy (0.356 mm Sn and 225 mg I/cm^2 filtration) and a high-energy (0.212 mm Cu filtration) spectra from a W-target exposed at 49 kV after transmission through a 6 cm 57% glandular equivalent breast.

Forty-eight projection images of 24×30cm^2 can be acquired within a single scan. The projection images are flat-field corrected. Tomographic reconstruction is performed using a simple filtered back-projection algorithm; tomographic images are reconstructed parallel with the detector array, spaced every 1 mm. The tomographic images are sixteen bits. The signal intensities in the tomographic images are linear with detector dose. The pixel size is 60 µm. As discussed in previous work, the imaging system is insensitive to scattered x rays; only x rays traveling in a straight line from the focal spot of the x-ray source can enter the detectors[17].

DECE tomographic images were produced that emphasize iodine contrast uptake in the breast. In the present analysis a weighted subtraction is applied to the logarithm of the high- and low-energy tomographic images.

$$I_{DE}(x,y) = \ln(I_H(x,y)) - w_t \cdot \ln(I_L(x,y)) \qquad (1)$$

where I_{DE} denotes the "iodine-enhanced" DECE tomographic image and, the subscripts L and H designate the low- and high-energy tomographic images. The tissue cancellation factor, w_t, acts as a weighting factor that maximizes the signal difference to noise ratio (SDNR) between the iodine contrast agent and the structured breast and that minimizes the variance in the structured breast tissue.

3. PHANTOM EXPERIMENTS

3.1. Structured Phantom Design

We designed two phantoms to evaluate the relationship between iodine contrast enhancement and structural background suppression in tomographic DECE images. The phantoms have 6 and 8 cm thick breast equivalent thicknesses. The 6 cm phantom has a 57% glandularity, the 8 cm phantom has a 55% glandularity. The breast equivalent thickness and glandularity were estimated by comparing the attenuation to known materials of the same thickness.

The phantom consists of two parts. One structured part is a 3.5 cm thick polymethyl metacrylate (PMMA) box filled with breast equivalent materials: extruded acrylic spheres simulate 50% glandular-50% fatty tissue, high density polyethylene spheres simulate pure fatty tissue and water simulates glandular tissue. The spheres have ½", ¼", ⅛" and ⅜" inch diameters and were homogeneously distributed in the box. The images of this structured part have the visual texture of a mammogram. The second part of the phantom consist of PMMA slabs in which iodine disks with various known surface concentrations (0.5, 1, 2, 4 mg/cm^2) are embedded. The iodine disks are 1.9 cm in diameter. The two parts were stacked such that the iodine disks were in contact with the structured portion.

3.2. Phantom Image Acquisition and Processing

The phantoms were scanned at 130 mA using all previously mentioned filter combinations and kVs. The performance of the DECE tomographic images of the phantom was compared as a function of mean glandular dose (MGD) absorbed in the phantom. Comparison was performed at a total MGD (MGD_{total}), the sum of the MGD allocated to the high- (MGD_H) and low-energy beam (MGD_L), of 2 mSv; this dose level corresponds to the typical MGD for a conventional mammogram. The fact that the same mA was applied for all kV-filter combinations caused differences in the MGD. To overcome this, various sets of projection images, each corresponding to a different dose level, were simulated for each investigated kV-filter combination. The simulated dose levels correspond to a multiple of the experimental applied dose used to image the phantom. A projection image corresponding to the ith dose level was obtained by applying an average sliding window filter: each pixel value (PV) in the experimentally obtained image was replaced by the average PV of that pixel and a sequence of (i-1)×1 neighboring pixels. Tomographic image sets were reconstructed as described above. The average sliding window filter was applied in the strip direction as the noise is uncorrelated in this direction. Figure 2 demonstrates the SNR as a function of dose level in flat-field projection images (Figure 2a) and corresponding tomographic images (Figure 2b) from x-ray beams filtered with various filters. This figure also demonstrates the SNR as a function of dose level when uncorrelated Poisson-distributed noise is considered in these images. The SNR in the projection images is ~15% lower for all dose levels than the SNR for uncorrelated Poisson noise. The SNR in the tomographic images is ~20% higher for all dose levels than the SNR for uncorrelated Poisson noise. We attribute these differences to sensitivity variations between detectors.

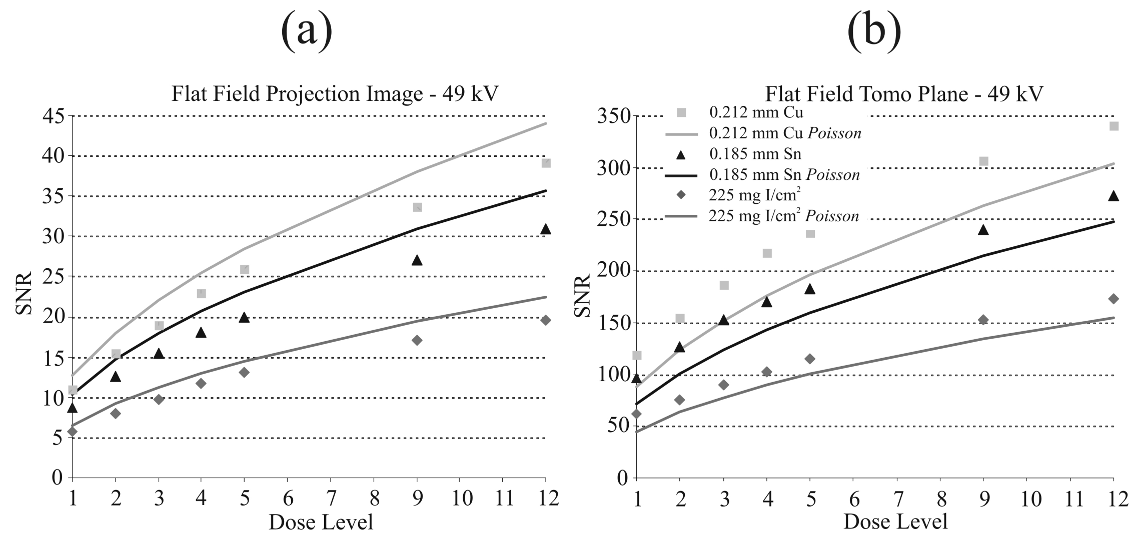

Figure 2: SNR as a function of dose level in (a) flat-field projection images of a 5 cm thick PMMA plate and (b) their reconstructions using various filters in the x-rays beam. The solid symbols correspond to the measured SNRs; the solid lines correspond to the SNRs assuming uncorrelated Poisson noise in these images.

The MGD in the breast equivalent phantoms were calculated for all investigated x-ray spectra at the experimentally applied and simulated dose levels by means of a model published by Boone[18]. This model requires knowledge of the breast entrance dose and the spectrum incident on the breast. Breast entrance doses were calculated from measured tube-outputs. Tube-outputs were measured by imaging an air ionization chamber with the same technical parameters used to image the phantoms. The ionization chamber was positioned at 4 cm from the table top (to reduce backscatter); the pre-collimator and compression plate were removed from the beam. The input spectra necessary for this calculation were simulated using a validated extrapolation of Boone's model for mammographic spectra[14].

3.3. Performance Optimization

3.3.1. Optimal Weighting Factor

The optimal w_t in the logarithmic subtraction was determined for each filter combination, kV and phantom thickness by varying w_t from 0 to 1 in steps of 0.01. The optimal value of w_t was obtained from the maximum signal difference to noise ratio (SDNR) between the iodine disks and the structured phantom background and the minimum variance in a "large area background" (2.5 by 2.5 cm^2). The calculations were performed in a tomographic plane with the iodine disks in focus.

3.3.2. Optimization for Dose

SDNR was computed in the DECE tomographic images as a function of the fraction of the MGD allocated to the high-energy beam, MGD_H/MGD_{Total}. The dose fraction allocated to the high-energy x-ray beam that maximizes the SDNR was evaluated. This calculation was computed at a MGD_{Total} = 2 mSv. The computations were performed for each filter combination, kV and phantom thickness. The optimal w_t was used for each experimental condition.

Despite the fact that some structure always remain in the DECE tomographic images of the structured phantom, even when the optimal w_t is applied, we estimated the SDNR one would get if this background was quantum noise limited:

$$SDNR_{FF} = \frac{\overline{SI}_{B\,DE} - \overline{SI}_{I\,DE}}{\sigma_{B_{DE}}} \qquad (3)$$

where $\overline{SI}_{B\,DE}$ and $\overline{SI}_{I\,DE}$ are the average SI in the background, B, and an iodine disk, I, of a DECE tomographic image; both SI were measured in the tomographic DECE images. $\sigma_{B_{DE}}$ is the quantum noise limited standard deviation in B of a tomographic DE image. The variance, $\sigma^2_{B_{DE}}$ can be written as the sum of the variances of B in the logarithm of the high, H, and low, L, energy images weighted by w_t^2:

$$\sigma^2_{B\,DE} = \sigma^2_{B\,H} + w_t^2 \sigma^2_{B\,L} \qquad (4)$$

Assuming uncorrelated Poisson noise, $\sigma_{B\,H}$ and $\sigma_{B\,L}$ can be calculated from the linear high- and low-energy images by applying the following existing relationship between the *SI* in these linear images and the logarithm of the *SI* of the linear images:

$$\sigma_{B\,E} = \frac{\ln(\overline{SI}_{B\,E\,lin})}{\ln(\overline{SI}_{B\,E\,lin}) \cdot \sqrt{DL \times \overline{SI}_{B\,E\,lin}} + \ln(DL)} \qquad (5)$$

where the subscript E refers to H or L; $\overline{SI}_{B\,E\,lin}$ is the mean *SI* in the linear images of B at energy E; and DL refers to the dose levels, described in Section 3.2. The dose level is incorporated in this equation because we applied an average filter to obtain images corresponding to various doses; as a consequence the mean *SI* in the simulated images does not vary with dose (by comparison, adding the *SI* would have resulted in a linear dependence with dose level). Using this method, $SDNR_{FF}$ will be underestimated by ~20%. This is because the standard deviation of the *SI* in the images (see Section 3.2 and Figure 2) deviate from the uncorrelated Poisson noise by ~20%.

The SDNR for a structured background, $SDNR_{Struct}$, was calculated as:

$$SDNR_{Struct} = \frac{\overline{SI}_{B\,DE} - \overline{SI}_{I\,DE}}{\sigma_{B_{DE\,struct}}} \qquad (6)$$

where $\sigma_{B_{DE\,struct}}$ is the standard deviation in $\overline{SI}_{B\,DE}$. $\sigma^2_{B_{DE\,struct}}$ was calculated along a line through the background in the strip direction. $SDNR_{Struct}$ takes both dose and anatomical noise into account. The strip direction was chosen to calculate $\sigma^2_{B_{DE\,struct}}$ to avoid noise correlation.

4. SIMULATION OF IMAGING SYSTEM

To confirm the predictions from our experimental measurements, we also modeled the experimental conditions using a previously presented extrapolation of the spectra of Boone[16]. The spectra were calculated for the photon counting imaging system operated at 45 kV and 49 kV with a W target. The raw W target spectra were shaped using the Lambert-Beer law with appropriate mass attenuation coefficients μ of the investigated low- and high-energy filters, air gap, compression plate and our composite phantoms. The simulated spectra were calibrated with respect to experimentally measured phantom entrance doses. The *SI* in the detector was calculated as the absorbed primary x-ray photon fluence per pixel. Uncorrelated Poisson noise was assumed. The mean *SI* in tomographic images was simulated by multiplying the absorbed primary x-ray fluence by 48. Our model ignored electronic noise and the effects of scatter; both are known to be small in the real system. The simulated absorbed *SI* was verified to be similar to the average *SI* in experimentally obtained flat-field projection images.

4.1. Performance Optimization

4.1.1. Optimal Weighting Factor

Using our imaging acquisition model, w_t was calculated to cancel optimally the contrast between adipose and fatty tissue in a tomographic DECE image. The optimal w_t was simulated for all experimentally investigated conditions; the various filter pairs, the 2 phantom thicknesses and as a function as kV. We assumed that the path of an x ray through the part of our composite phantoms that contains the spheres may vary from traveling through pure glandular tissue to traveling through pure fat. We simulated x rays being attenuated by 3 cm thick 0% (100%), 25% (75%), 50% (50%) and 100% (0%) glandular tissue (fat). The optimal w_t was calculated as[13]:

$$w_t = \frac{\ln(H_1(E)) - \ln(H_2(E))}{\ln(L_1(E)) - \ln(L_2(E))} \qquad (7)$$

$H_1(E), H_2(E), L_1(E)$ and $L_2(E)$ are given by:

$$H_1(E) = \int_E d(E) S_H(E) e^{-\mu_{PMMA}(E) t_{PMMA} - \mu_g(E) ff_{g1} L_{Struct} - \mu_f(E)(1-ff_{g1}) L_{Struct}} (1 - e^{-\mu_{Gas}(E) t_{Gas}}) dE \qquad (8)$$

$$H_2(E) = \int_E d(E) S_H(E) e^{-\mu_{PMMA}(E) t_{PMMA} - \mu_g(E) ff_{g2} L_{Struct} - \mu_f(E)(1-ff_{g2}) L_{Struct}} (1 - e^{-\mu_{Gas}(E) t_{Gas}}) dE \qquad (9)$$

$$L_1(E) = \int_E d(E) S_L(E) e^{-\mu_{PMMA}(E)(E) t_{PMMA} - \mu_g(E) ff_{g1} L_{Struct} - \mu_f(E)(1-ff_{g1}) L_{Struct}} (1 - e^{-\mu_{Gas}(E) t_{Gas}}) dE \qquad (10)$$

$$L_2(E) = \int_E d(E) S_L(E) e^{-\mu_{PMMA}(E) t_{PMMA} - \mu_g(E) ff_{g2} L_{Struct} - \mu_f(E)(1-ff_{g2}) L_{Struct}} (1 - e^{-\mu_{Gas}(E) t_{Gas}}) dE \qquad (11)$$

where subscripts 1 and 2 refer to two paths of x rays through the composite phantom. The integrals $\int S_H(E)dE$ and $\int S_L(E)dE$ denote the high- and low-energy spectrum normalized to unity; *Gas* refers to the gas in the detector, *f* refers to fat tissue; *g* refers to glandular tissue; L_{Struct} is the thickness of the structured part of our phantom; t_{PMMA} is the thickness of the PMMA slabs in the composite phantom; ff_{g1} and ff_{g2} are the fractions of glandular tissue along x-ray paths 1 and 2 through the structured part of the phantom. The values of w_t that produce optimal tissue cancellation were calculated for ffg_1 equal to 0, 0.25, 0.5 and 1. Note that w_t is independent of dose; in practice this will hold as long as structured noise dominates quantum noise.

4.1.2. Optimization for Dose

Using our simulation model, we calculated $SDNR_{FF}$ in the DECE tomographic images as a function of MGD_H/MGD_{Total}. The MGD_H/MGD_{Total} that results in a maximum $SDNR_{FF}$ was evaluated. The calculation was repeated for all experimental conditions. The optimal w_t was used for each condition. Our simulations were performed for a MGD_{Total} = 2 mSv.

5. RESULTS AND DISCUSSION

5.1. Optimal Weighting Factor

Figure 3 illustrates the SDNR and structured background variance in a tomographic DECE image as a function of w_t for the 6 cm thick 57% glandular-equivalent breast exposed at 49 kV with a W target using a 0.356 mm Sn - 0.212 mm Cu filter pair. The magnitude of the SDNR and large area background variance vary significantly as a function of w_t; *SDNR* is maximized and the large area background variance is minimized at w_t = 0.58. We have performed this calculation for all investigated low- and high-energy filter combinations, breast thicknesses and kVs. Figure 4 shows optimal w_t values as a function of filter combination, kV and phantom thickness. The optimal w_t values are derived from both experiments and simulation. The w_t values from simulation did not differ when different ff_{g1} values were used in equation (7). There is very good agreement between the experimentally derived and simulated values. Optimal w_t are in the range 0.5-0.82. The optimum w_t depends mainly on the filter pair: the optimal w_t for iodine-Cu filters is larger than the optimal w_t for Sn-Cu filters. The optimal w_t varies only slightly with tube voltage and breast thickness. These preliminary results are very encouraging for a clinical DECE-DBT system with fixed filter combination, since the same w_t can be used for all breast types.

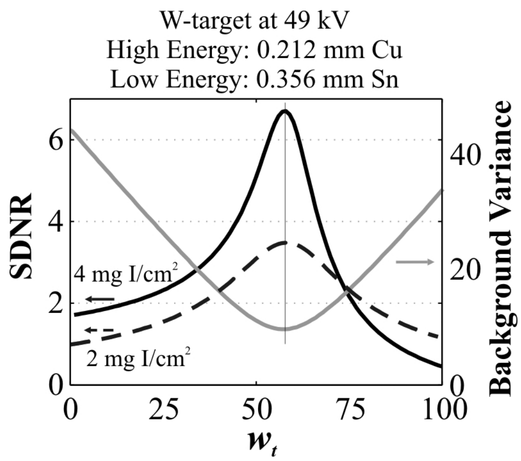

Figure 3: SDNR and large area background variance as a function of tissue cancellation factor w_t. SDNR; a measure of iodine contrast, and background variance; a measure of removal of the structured background, are optimal for $w_t = 0.58$.

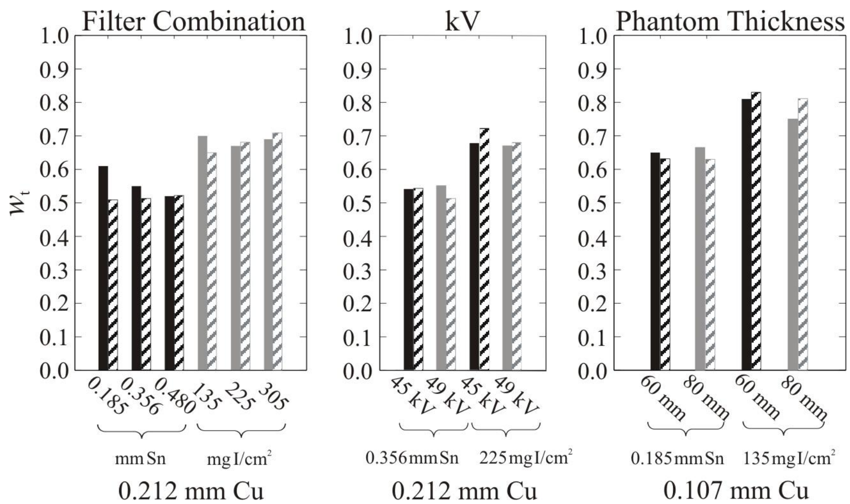

Figure 4: Optimal w_t as a function of filter combination, kV and phantom thickness. Note that the optimal w_t of the Sn-Cu combinations is smaller than the optimal w_t for the I-Cu combinations. The optimal w_t varies only slightly with kV and phantom thickness. Solid bars are experimentally derived w_t values, striped bars are theoretically calculated w_t values.

5.2. Optimization for Dose

Figure 5 illustrates the optimization for MGD_H/MGD_{Total}. Figure 5a shows both experimental and simulated $SDNR_{FF}$ values when various Cu thicknesses are used to obtain the high-energy images and a fixed Sn filter thickness is used to obtain the low-energy images. The maximum difference between the simulated and the experimental $SDNR_{FF}$ values is ~15%. A fairly strong dependence is observed in $SDNR_{FF}$ on MGD_H/MGD_{Total}. Maximum $SDNR_{FF}$ values were found for MGD_H/MGD_{Total} ranging from 0.55 to 0.65; the optimum MGD_H/MGD_{Total} seems to increase for thicker Cu filters. The optimal MGD_H/MGD_{Total} is independent of MGD_{Total} (not shown). Figure 5b compares $SDNR_{FF}$ and $SDNR_{Struct}$ for a 0.27 mm Cu filter– 0.356 mm Sn filter pair. $SDNR_{FF}$ and $SDNR_{Struct}$ are very similar as a function of MGD_H/MGD_{Total}. Note that $SDNR_{Struct}$ drops more gradually as MGD_H/MGD_{Total} approaches one. This can be explained by the fact that structured noise dominates the quantum noise at higher MGD_H/MGD_{Total} values. Note that using our DECE-DBT design, the high- and low-energy images are acquired in a single scan. It is therefore impossible to simultaneously maximize $SDNR_{FF}$ and $SDNR_{Struct}$ for any filter pair; the optimal MGD_H/MGD_{Total} can only be obtained if the high- and low-energy images are acquired with a different mA. Therefore, we will optimize our DECE-DBT system by choosing a filter pair for which the optimal MGD_H/MGD_{Total} can be obtained.

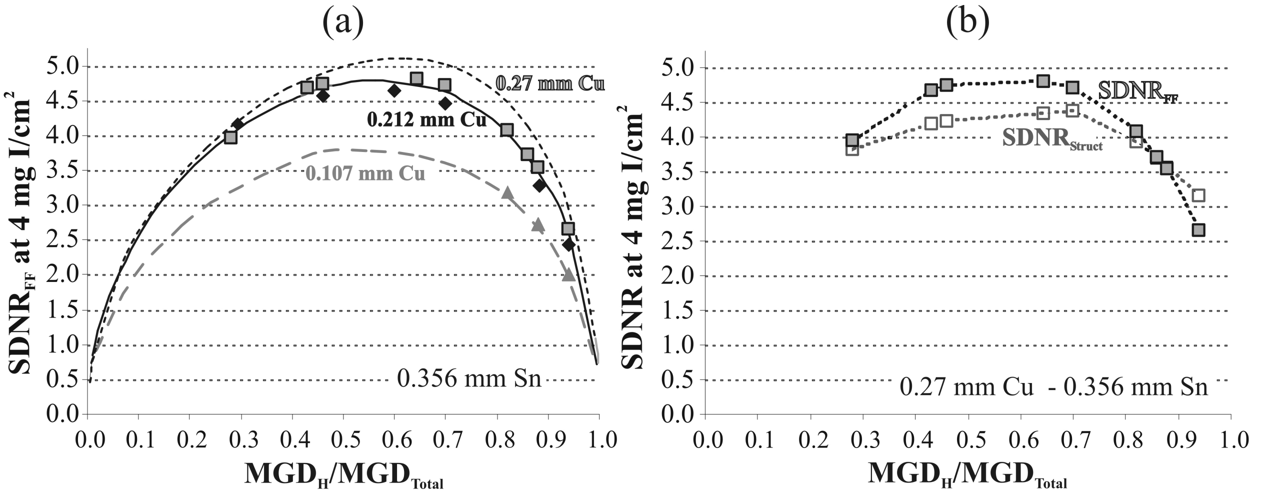

Figure 5: (a) SDNR$_{FF}$ in DECE tomographic images as a function of MGD$_H$/MGD$_{Total}$. Cu filters of various thicknesses were used to obtain high-energy images and a 0.356 mm thick Sn filter was used to obtain low-energy images. The solid symbols correspond to experimentally derived SDNR$_{FF}$ values; the lines correspond to SDNR$_{FF}$ values from simulating the imaging process. The experimental and theoretical values differ by a maximum of 15%. (b) Comparison of SDNR$_{FF}$ and SDNR$_{FF}$ values as a function of MGD$_H$/MGD$_{Total}$.

Figure 6 shows the SDNR$_{FF}$ (Figure 6a) and SDNR$_{Struct}$ (Figure 6b) in DECE tomographic images of the 6 cm thick phantom when the low- and high-energy images are acquired with various Cu and Sn filter thicknesses and optimal w_t and MGD$_H$/MGD$_{Total}$ are applied for the logarithmic subtraction. The calculations were made with a MGD$_{Total}$ = 2mSv. SDNR$_{FF}$ increases for thicker Cu and Sn filters. For a fixed low-energy filter thickness, the SDNR$_{FF}$ increases most when going from 0.107 mm Cu to 0.212 mm Cu. The advantage of the 0.27 mm Cu filter is marginal. Similarly, for a given Cu filter thickness, SDNR$_{FF}$ increase most when switching from a 0.185 mm Sn filter to a 0.356 mm Sn filter. Note that SDNR$_{FF}$ values are underestimated by ~20%. For a given low-energy filter thickness, SDNR$_{Struct}$ is highest for the intermediate (0.212 mm) Cu filter. Similarly, for a given high-energy filter thickness, SDNR$_{Struct}$ is highest for the intermediate (0.356 mm) Sn filter.

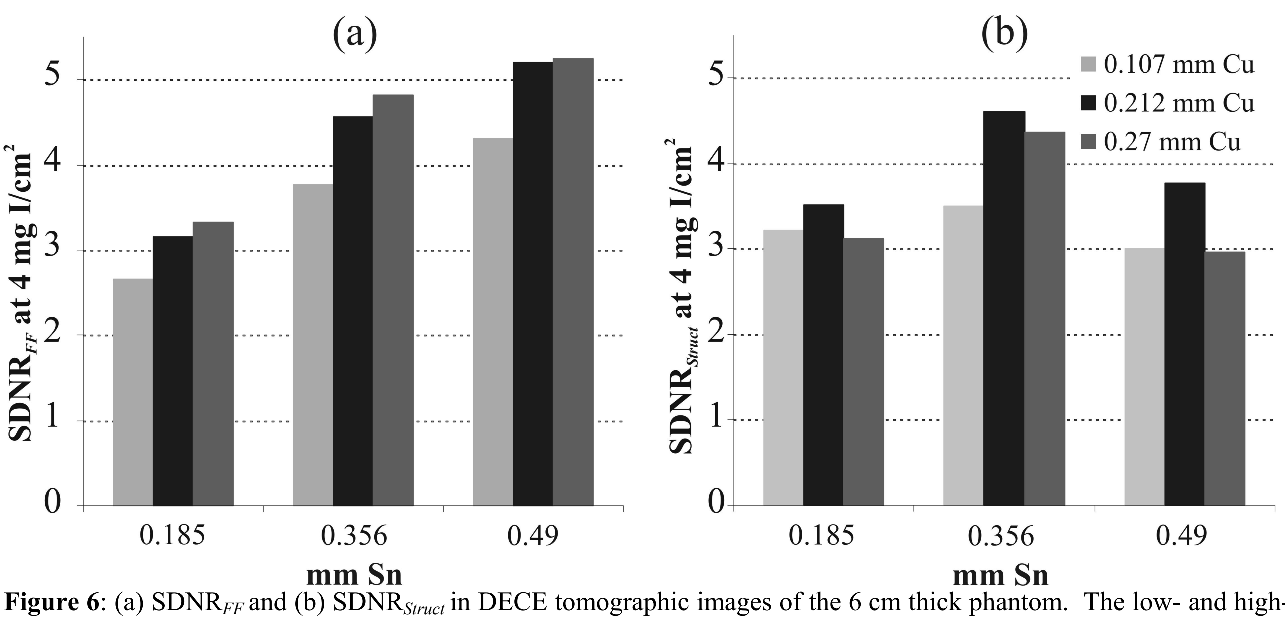

Figure 6: (a) SDNR$_{FF}$ and (b) SDNR$_{Struct}$ in DECE tomographic images of the 6 cm thick phantom. The low- and high-energy images were acquired with various Cu and Sn filter thicknesses. The phantom was imaged with a W- target at 49 kV. Optimal w_t and MGD$_H$/MGD$_{Total}$ values were used. MGD$_{Total}$ = 2mSv.

Figure 7 shows the $SDNR_{FF}$ (Figure 7a) and $SDNR_{Struct}$ (Figure 7b) in DECE tomographic images of the 6 cm thick phantom when the low-energy images are acquired with 135 mg I/cm^2 and 0.185 mm Sn filters and the 0.107 mm Cu filter was used for the high-energy images. Optimal w_t and MGD_H/MGD_{Total} are applied for the logarithmic subtraction and MGD_{Total}=2mSv. $SDNR_{FF}$ increases from 2.7 to 3.3 when switching from Sn to the iodine filter. The advantage of the iodine filter is not as large in the $SDNR_{Struct}$. Figure 8 compares $SDNR_{FF}$ and $SDNR_{Struct}$ in DECE tomographic images of the 6 cm thick phantom acquired at 45 kV and 49 kV using a 0.212 mm Cu – 0.356 mm Sn filter combination. $SDNR_{FF}$ and $SDNR_{Struct}$ only vary slightly with kV. Figure 9 shows a high-energy (0.212 mm Cu filter) and a low-energy (0.35 mm Sn filter) image and DECE tomographic image of a structured phantom acquired with a W target at 49 kV. Optimal values for w_t and MGD_H/MGD_{Total} were used. The MGD_{Total} = 2mSv. Iodine concentrations down to 1 mg/cm^2 are quite conspicuous.

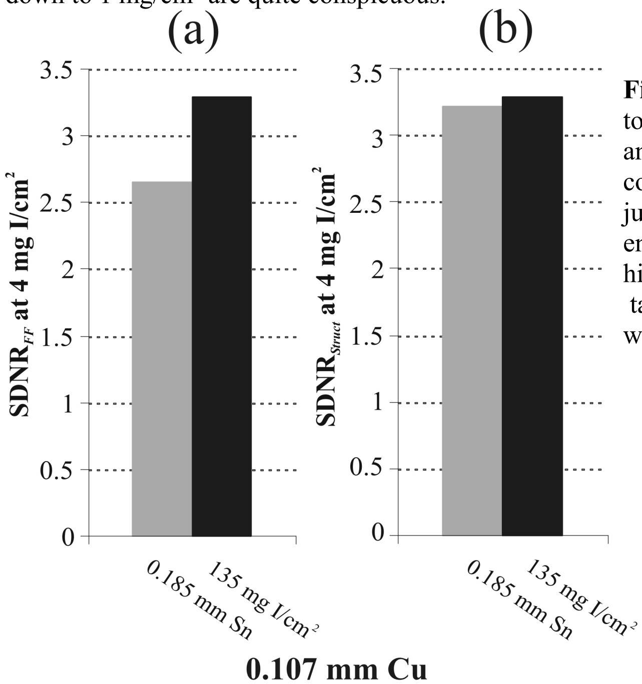

Figure 7: (a) $SDNR_{FF}$ and (b) $SDNR_{Struct}$ in DECE tomographic images of the 6 cm thick phantom when using an iodine (with K-edge that matches the K-edge of the contrast agent) versus a Sn filter (with K-edge at 29,2 keV; just below the K-edge of the contrast agent) for the low-energy images. A 0.107 mm Cu filter was used for the high-energy images. The phantom was imaged with a W-target at 49 kV. Optimal w_t and MGD_H/MGD_{Total} values were used. MGD_{Total} = 2mSv.

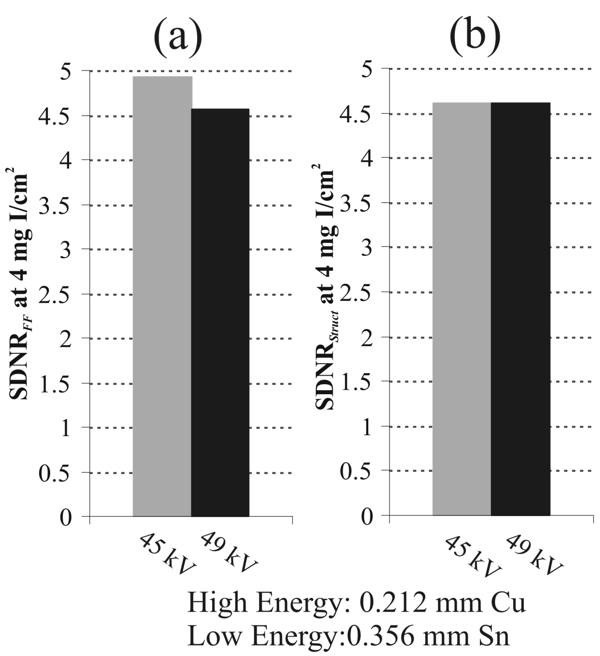

Figure 8: (a) $SDNR_{FF}$ and (b) $SDNR_{Struct}$ in DECE tomographic images of the 6 cm thick phantom when the images are acquired at 45 kV versus 49 kV. The phantom was imaged with a W-target at 49 kV using 0.212 mm Cu filter for the high-energy images and 0.356 mm Sn filter for the low-energy images. Optimal w_t and MGD_H/MGD_{Total} values were used. MGD_{Total} = 2mSv.

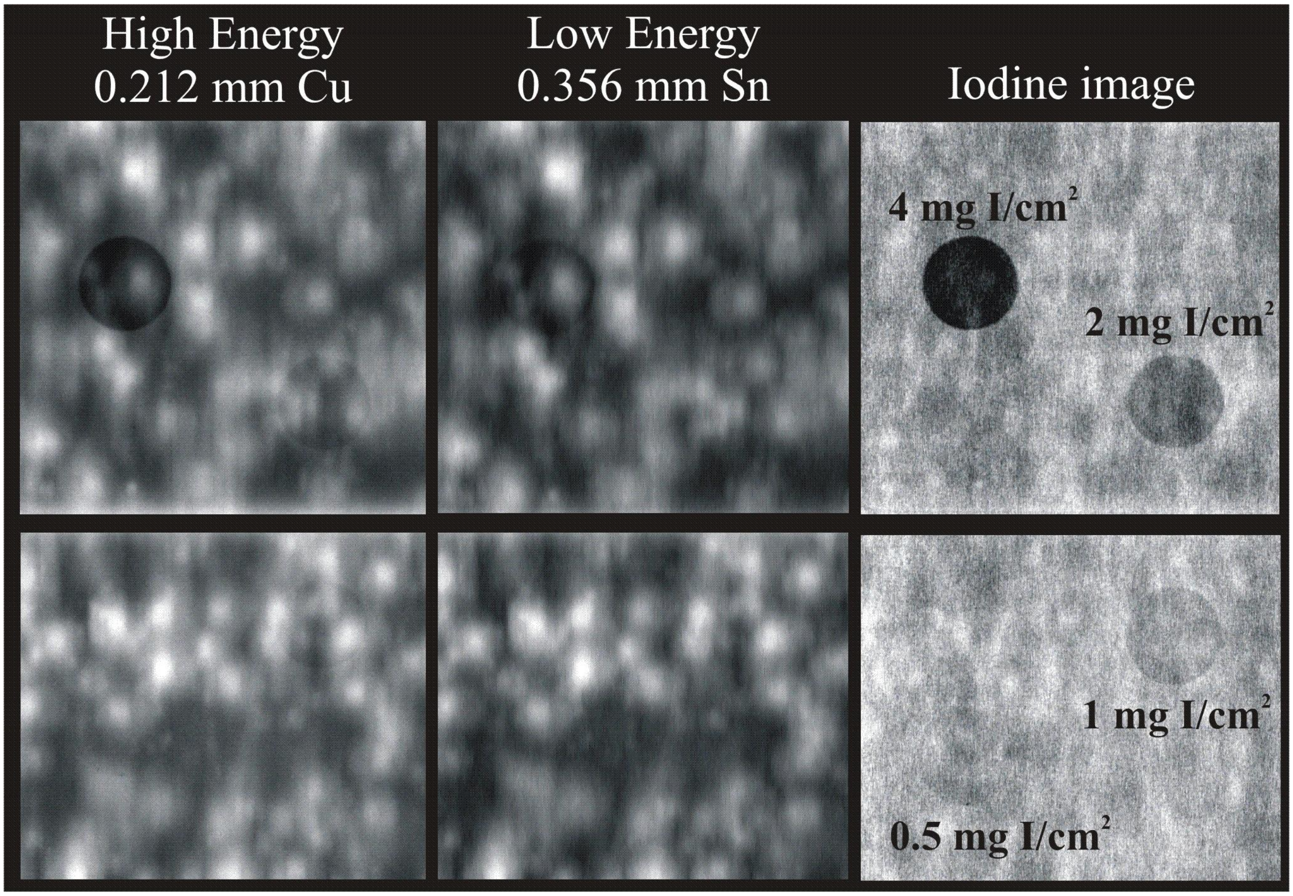

Figure 9: Reconstructed DBT slice of the composite phantom acquired with a high- (left) and low-energy spectrum (middle). The image at the right is the DECE tomographic image (optimal w_t= 0.58). Note that iodine concentrations down to 1 mg/cm^2 are quite suspicious.

6. CONCLUSION

We explored the technical requirements for performing DECE-DBT when the high- and the low-energy images are acquired in a single scan and at the same kV. We have conducted both phantom experiments and theoretical modeling. The results from modeling the imaging system are very similar to the experimentally obtained results. We succeeded in simulating the noise in the images, the optimal tissue cancellation factor, and the optimal dose distribution between the high- and low-energy beams that result in maximum SDNR in quantum-noise and structured-noise limited images. These results will allow us to further optimize the proposed DECE-DBT system using simulations.

Cu was used to filter the high-energy images; iodine and Sn were used to filter the low-energy images. Iodine was chosen because the K-edge of this filter matches the K-edge of the contrast agent. We investigated Sn filters (K-edge at 29.2 keV) because they are readably available in solid form; our iodine filters were liquid. An outstanding challenge is to find an appropriate solid iodine filter.

We are aware of 4 DECE studies of the breast[11-13,19]. Bornefalk[12] demonstrated the ability to visualize a 1.5 mg I/cm^2, 1 cm in diameter insert in a 4.5 cm thick, 50% glandular breast equivalent phantom using a 1.42 mSv MGD with a differential beam splitting technique. A 0.93 mg I/cm^2 insert could be visualized in a 2.7 cm thick, 50% glandular phantom using a differential beam splitting technique[13]. Baldelli[19] has shown an SDNR = 5 for a 4.13 mg I/cm^2, 0.8 cm in diameter cavity and 5.74 mg I/cm^2, 0.5 cm in diameter cavity in a 5.6 cm thick, 25% glandular breast equivalent phantom using a 4.27 mSv MGD. These results are comparable to our results. Temporal subtraction appears to be more sensitive; Baldelli[19] has shown that a 1.01 mg I/cm^2, 0.8 cm in diameter cavity and a 1.57 mg I/cm^2, 0.5 cm in diameter cavity resulted in an SDNR = 5. But, as we have shown, temporal subtraction DECE-DBT is very sensitive to motion artifacts[14].

In future work, we will investigate how to quantify iodine contrast-agent uptake and we will explore noise reduction algorithms.

7. ACKNOWLEDGMENT

We like to thank the financial support of Phillips Medical Systems/RSNA Research Seed Grant 2005, the Department of Defense for the Concept Award BC052803 and the National Cancer Institute Grant PO1-CA85484.

8. REFERENCES

1. N. Weidner, J.P. Semple, W.R. Welch & J. Folkman. Tumor angiogenesis and metastasis: correlation in invasive breast carcinoma. *New England Journal of Medicine* **324**, 1-8 (1991).
2. C. Boetes, J.O. Barentsz, R.D. Mus, R.F. van der Sluis, L.J. van Erning, J.H. Hendriks, R. Holland & S.H. Ruys. MR characterization of suspicious breast lesions with a gadolinium-enhanced TurboFLASH subtraction technique. *Radiology* **193**, 777-781 (1994).
3. W.A. Kaiser & E. Zeitler. MR imaging of the breast: fast imaging sequences with and without Gd-DTPA. Preliminary observations. *Radiology* **170**, 681-686 (1989).
4. S. Mussurakis, D.L. Buckley, S. Bowsley, P.J. Carleton, J.N. Fox, L.W. Turnbull & A. Horsman. Dynamic contrast-enhanced magnetic resonance imaging of the breast combined with pharmacokinetic analysis of gadolinium-DTPA uptake in the diagnosis of local recurrence of early stage breast carcinoma. *Investigative Radiology* **30**, 650–662 (1995).
5. F. Sardanelli, G. Rescinito, G.D. Giordano, M. Calabrese & R.C. Parodi. MR dynamic enhancement of breast lesions: high temporal resolution during the first-minute versus eight-minute study. *Journal of Computed Assisted Tomography* **24**, 724-731 (2000).
6. L.V. Ackerman, A.C. Watt, P. Shetty, M.J. Flynn, M. Burke, A. Kambouris, G. Fine & S. Wilderman. Breast lesions examined by digital angiography. Work in progress. *Radiology* **155**, 65-8 (1985).
7. A.C. Watt, L.V. Ackerman, J.P. Windham, P.C. Shetty, M.W. Burke, M.J. Flynn, C. Grodinsky, G. Fine & S.J. Wilderman. Breast lesions: differential diagnosis using digital subtraction angiography. *Radiology* **159**, 39-42 (1986).
8. J.L. Sibala, J. Chang, F. Lin & W.R. Jewell. Computed tomographic mammography. *Arch Surg* **116**, 114-117 (1981).
9. S.L. Fritz, C.H.J. Chang & W.H. Livingston. Scatter/primary ratio for x-ray spectra modified to enhance iodine contrast in screen-film mammography. *Medical Physics* **10**, 866-870 (1983).
10. R.A. Jong, M.J. Yaffe, M. Skarpathiotakis, R.S. Shumak, N.M. Danjoux, A. Gunesekara & D.B. Plewes. Contrast-enhanced digital mammography: Initial clinical experience. *Radiology* **228**, 842-850 (2003).
11. J.M. Lewin, P.K. Isaacs, V. Vance & F.J. Larke. Dual-energy contrast-enhanced digital subtraction mammography: Feasibility. *Radiology* **264**, 261-268 (2003).
12. H. Bornefalk, M. Hemmendorff & T. Hjarm. Dual-energy imaging using a digital scanned multi-slit system for mammography: evaluation of a differential beam filtering technique. *Medical Imaging 2006: Physics of Medical Imaging* **6142**, 614220-1-614220-7 (2006).
13. H. Bornefalk. Computer-aided detection and novel mammography imaging techniques, PhD. thesis, *Department of Physics* 417 (Royal Institute of Technology, Stockholm, 2006).
14. A.-K. Carton, J. Li, M. Albert, S. Chen & A.D. Maidment. in *Medical Imaging 2006: Physics of Medical Imaging* (eds. Flynn, M. J. & Hsieh, J.) 111-121 (San Diego, 2006).
15. A.D.A. Maidment & M. Albert. in *Advances in digital mammography: categorical course in diagnostic radiology physics* (eds. Samei, E. & Flynn, M. J.) 252 (Radiological Society of North America, 2003).
16. J.M. Boone, T.R. Fewell & R.J. Jennings. Molybdenum, rhodium, and tungsten anode spectral models using interpolating polynomials with application to mammography. *Medical Physics* **24**, 1863-74 (1997).
17. A.D.A. Maidment, M. Albert, S. Thunberg, L. AdelÖw, O. Blom, J. EgerstrÖm, M. Eklund, T. Francke, U. Jordung, T. Kristoffersson, K. Lindman, L. Lindqvist, D. Marchal, H. Olla, E. Penton, J. Rantanen, S. Solokov, C. Ullberg & N. Weber. in *SPIE* (ed. Flynn, M. J.) 572-82 ((SPIE, Bellingham, WA, 2005), San Diego, CA, 2005).

18. J.M. Boone. Glandular breast dose for monoenergetic and high-energy X-ray beams: Monte Carlo assessment.[see comment]. *Radiology* **213**, 23-37 (1999).
19. P. Baldelli, A. Bravin, C. Di Maggio, G. Gennaro, A. Sarnelli, A. Taibi & M. Gambaccini1. Evaluation of the minimum iodine concentration for contrast-enhanced subtraction mammography. *Physics in Medicine and Biology* **51** (2006).